DNA origami directed integration of colloidal nanophotonic materials with silicon photonics

Xin Luo[1, 2], Luigi Ranno[2], Tara Sverko[3], Jae Young Lee[1], Nicholas Sbalbi[2], Annette Jones[3], Chi Chen[1], Moungi G. Bawendi[3], Juejun Hu[2], Robert J. Macfarlane[2]*, Mark Bathe[1]*

Affiliations

[1]Department of Biological Engineering, Massachusetts Institute of Technology, Cambridge, MA, 02139, USA.

[2]Department of Materials Science and Engineering, Massachusetts Institute of Technology, Cambridge, MA, 02139, USA.

[3]Department of Chemistry, Massachusetts Institute of Technology, Cambridge, MA, 02139, USA.

* Corresponding author emails: mark.bathe@mit.edu, rmacfarl@mit.edu

Abstract

Deterministic incorporation of colloidal quantum emitters into silicon-based photonic devices would enable major advances in quantum optics and nanophotonics. However, precisely positioning sub-10 nm particles onto micron-sized photonic structures with nanometer-scale accuracy remains an outstanding challenge. Here, we introduce Cavity-Shape Modulated Origami Placement (CSMOP) that leverages the shape programmability of DNA origami to selectively deposit colloidal nanomaterials within lithographically defined resist cavities patterned onto arbitrary photonic devices with high yield and orientation control. Soft-silicification-passivation stabilizes the deposited origami, while preserving their spatially programmable DNA hybridization sites, which enable site-specific attachment of plasmonic gold nanorods (AuNRs) and semiconductor quantum rods (QRs). This offers control over light scattering and emission polarization, respectively, with deterministic integration of individual QRs within silicon nitride waveguides, micro-ring resonators, and bullseye cavities. CSMOP thereby offers a general platform for the integration of colloidal nanomaterials into photonic circuits, with broad potential to empower quantum information science and technology.

Main Text

Advances in nanophotonic research and technology, such as metasurfaces and photonic integrated circuits (PICs), demand precise and selective nanoscale spatial control over the fabrication of optically functional materials, particularly for cutting-edge applications like quantum optics[1-3]. Conventional top-down fabrication techniques, however, are limited by their fabrication resolution, scalability, and uniformity[4-8]. Alternatively, bottom-up synthesis through molecular and colloidal

approaches can scalably produce diverse libraries of high-quality optical nanomaterials with nanometer or even sub-nanometer structural features that possess tunable optical properties and efficiently engineered functionalities[9-14]. Despite the potential of bottom-up approaches for photonic materials production, colloidal nanomaterials exhibit a key challenge that limits their utility: they are synthesized stochastically in solution, but their implementation into practical devices requires their deterministic, single-particle incorporation within fabricated optical and electronic structures on-chip. For example, precisely organizing single-photon emitting colloidal quantum emitters on PICs could unlock a broad spectrum of applications in quantum sensing, communication and computing[15-18]. However, most methods for integrating colloidal nanomaterials into PICs predominantly rely on inefficient processes such as post-deposition fabrication[19-22] or direct lithography-guided stochastic deposition[23-28], limiting advances in their application to basic research and device fabrication. Capillary force-assisted techniques can improve placement efficiency, but they are typically limited to large NPs on flat substrates with size-matching traps that do not offer programmable selectivity[29-34]. Thus, achieving precise, selective, and scalable integration of colloidal nanomaterials smaller than 10 nm—which is typical of quantum emitters—into micron-scale topographically defined photonic structures with nanoscale control remains an important unsolved challenge.

DNA nanotechnology, particularly DNA origami, has recently emerged as a scalable bottom-up approach to organize nanoscale optical materials in a multiplexed manner, including molecular emitters[35-37], metallic nanoparticles (NPs)[38-40], upconversion NPs[41], quantum dots (QDs)[42-46] and nanodiamonds[47, 48] into complex hierarchical structures with sub-nanometer scale accuracy. While DNA nanostructures are typically restricted to solution-based assemblies, pioneering work developed the DNA Origami Placement (DOP) method where 2D[49-52] and 3D[53] DNA origami objects were precisely positioned via electrostatic interactions onto landing pads defined by electron beam lithography (EBL) on a silicon substrate. While the DOP method has been used to successfully organize dye molecules[51, 52] and gold nanospheres (AuNSs)[53, 54], which can be made colloidally stable in the high ionic strength solutions required for DNA origami placement, metastable colloids with unique optical properties of high value such as nanodiamonds and quantum rods (QRs) are not amenable to such approaches. Furthermore, while alternative lithography methods have been explored to guide DNA origami placement on various flat substrates[55-60], little progress has been made towards integrating individual colloidal optical nanomaterials with practical PIC structures, such as waveguides and micro-ring resonators, where micron-scale topographical features can hinder precise DNA origami placement and lead to random trapping of nanomaterials in undesired locations on the device, thereby diminishing its functionality.

Here, we introduce Cavity-Shape Modulated Origami Placement (CSMOP) that enables the precise integration of individual colloidal nanomaterials into photonic devices by leveraging lithographic patterning with the unique ability of DNA origami to control colloidal nanomaterials (**Fig. 1**). Specifically, CSMOP uses EBL to define origami shape-matching cavities in a resist layer, whereby cavity-origami interactions are modulated via topographical confinement, ionic conditions, and origami shape design to achieve accurate placement of origami including control over nanometer-scale spatial position and orientation. DNA origami objects are designed with hybridization overhangs that enable subsequent capture of DNA-functionalized nanomaterials to control their spatial position and orientation on the patterned substrate. Using this platform, we demonstrated high-yield assembly of AuNS arrays and orientation-controlled placement of gold

nanorods (AuNRs) to control anisotropic light scattering. Additionally, we established a soft-silicification-passivation strategy that stabilizes CSMOP origami attachment while preserving DNA hybridization capability to assemble QRs in the lower ionic strength conditions required for their colloidal stability. We show that CSMOP enables the deterministic placement of individual QRs on silicon nitride (SiN_x) waveguides, micro-ring resonators, and bullseye cavities. After depositing QRs and removing the EBL resist, these QR arrays exhibit controlled emission polarization and minimal background emission due to the selective positioning of QRs within the subsequently removed resist cavities. Thus, CSMOP provides a general platform for precise incorporation of colloidal quantum emitters into photonic integrated circuits, offering valuable new opportunities for quantum information science and technology using photon-based quantum sensing [61], computing [62], and communication [63].

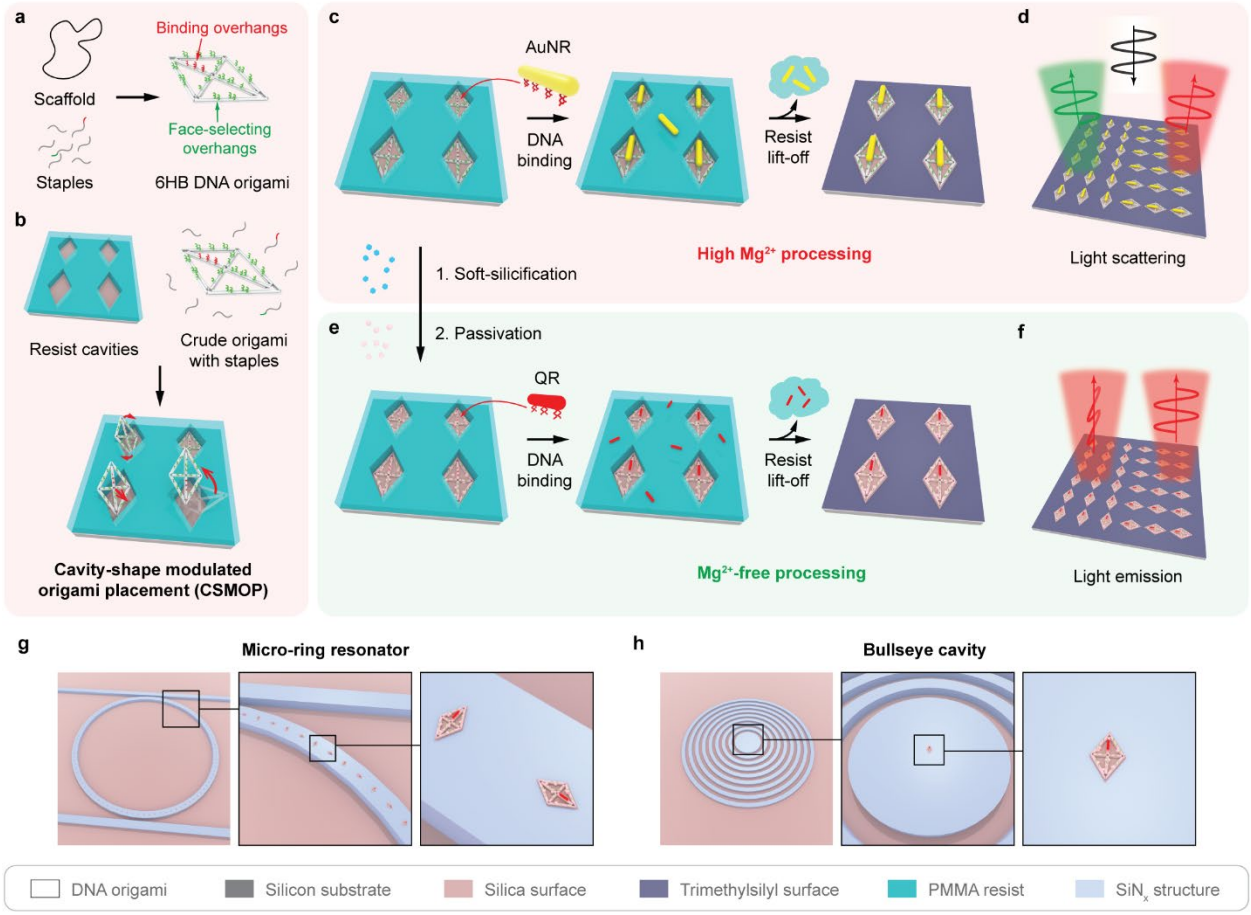

Fig. 1. Overview of CSMOP and its application to nanoscale patterning of AuNRs and QRs. a, Design and assembly of planar DNA origami. **b**, Cavity-shape modulated placement of origamis with binding overhangs facing up at the base of EBL-defined cavities in the PMMA resist. **c**, AuNR attachment and alignment to CSMOP-directed origami within the cavity under high Mg^{2+} concentration. **d**, Illustration of a CSMOP-directed AuNR array with controlled plasmonic light scattering. **e**, Soft-silicification and passivation of origami within the cavity to attach and align QRs under Mg^{2+}-free conditions. **f**, Illustration of a CSMOP-directed QR array with controlled emission polarization. **g–h**, CSMOP enabled deterministic integration of individual QRs within micro-ring resonators (g) and bullseye photonic cavities (h) with positional and orientational control. Surface chemical modifications were omitted in **g** and **h**.

Cavity-shape modulated origami placement

CSMOP uses topographical cavities in the resist layer to modulate DNA origami placement and subsequent nanomaterial integration; the use of a 3D cavity to define origami positioning provides two key advantages over the previous approach[51, 52]. First, the resist layer prevents random attachment of nanomaterials to a substrate or device, as it provides a physical barrier for all regions upon which colloidal materials should not deposit. Unintentional accumulation of nanomaterials is thereby easily cleared by dissolving the resist and washing away NPs that are not directly attached to the substrate. Second, shape-matching confinement with the topographical cavity can help regulate origami orientation and minimize aggregation, which has been tested using large NPs[34, 64, 65] and origami on diamond-like carbon[49]. We fabricated origami-shape matching cavities within a poly(methyl methacrylate) (PMMA) resist layer using a standard EBL process (see **Methods** and **Supplementary Fig. 1**). After recovering the hydrophilic silica surface at the base of the cavities with anisotropic O_2 plasma etching, the negatively charged surface hydroxyl groups in solution allowed for Mg^{2+}-bridged DNA origami binding.

We hypothesized that structural flexibility and deformation would increase unwanted origami landing conformations in the cavity, and therefore employed 2D six-helix bundle (6HB) wireframe origamis (**Supplementary Fig. 2** and **Supplementary Note 1**) as the model platform for CSMOP to take advantage of their planarity and rigidity[66, 67]. In addition, wireframe structures reduce the effective interaction area between the substrate and the origami compared with conventional single-layered structures, which are also more flexible. We anticipated that this reduced binding interaction would lead to more dynamic binding of the origami to the substrate, which could improve error correction during the placement process. To permit the capture of DNA-functionalized nanomaterials after origami deposition, one side of the origami was functionalized with single-stranded DNA (ssDNA) overhangs of two sequences: the NP binding sequence (**Fig. 1a**, red) and 20-nucleotide polythymidine (**Fig. 1a**, green). Because ssDNA overhangs can act as entropic brushes to prevent binding of the functionalized origami face to the substrate[43, 52], this design ensured the upward-facing orientation of the origami face with accessible NP binding strands following CSMOP.

We first tested CSMOP using a rhombic 6HB wireframe origami structure with short and long diagonal axes of approximately 75 nm and 125 nm, respectively. The origami was assembled and adjusted to 1 nM in buffer containing 35 mM $MgCl_2$ prior to silicon chip deposition (see **Methods**). Notably, the CSMOP method proved effective using crude, unpurified origami in solution, eliminating the need for purification of the origami following self-assembly and prior to their surface-deposition. This simplification not only streamlined the workflow but also avoided material loss and origami aggregation that is commonly associated with purification processes[68, 69]. In a typical CSMOP process, a crude rhombic origami solution was applied to a 0.5 cm × 1 cm chip bearing EBL-fabricated rhombic-shaped cavity arrays (**Fig. 2a**, left; **Supplementary Fig. 3**). The chip with origami solution was incubated at 23 °C for 2 h in a humid environment, followed by sequential washing with buffers to remove excess DNA origami and staple strands (see **Methods**). Atomic force microscopy (AFM) revealed rhombic origamis located at the cavity bases of the chip (**Fig. 2a**, middle; **Supplementary Fig. 4**). Subsequent PMMA lift-off, achieved using ultrasonication in *N*-methylpyrrolidone (NMP), removed the resist layer and background residuals from the dried origami solution, leaving only the cavity-directed origami structures on the substrate

(**Fig. 2a**, right; **Supplementary Fig. 5**). Origami silicification prior to lift-off rendered the origami structures robust and visible under scanning electron microscopy (SEM) (see **Methods**). Using this approach, we fabricated a 5.5 μm × 5 μm silicified CSMOP array, comprising six strips of rhombic origamis oriented vertically (i, ii, iii) or horizontally (iv, v, vi) with inter-origami spacings of 250 nm (i, vi), 500 nm (ii, v), or 1 μm (iii, iv) (**Fig. 2b**, **Supplementary Figs. 6–7**). No background contamination was observed by SEM imaging after the lift-off process, highlighting both the scalability and high yield of CSMOP.

It is important to note that DNA origami has the unique ability to fabricate nanostructures of arbitrary, well-defined geometries on the 10–100 nm scale, providing diverse templates for selective and orthogonal incorporation of colloidal nanomaterials with distinct properties. Thus, to further demonstrate the versatility of the CSMOP method, both a ladder-shaped 6HB wireframe origami and a commonly used single-layer triangular origami were prepared and deposited using CSMOP (**Supplementary Figs. 8–12**). These additional origami shapes were also amenable to CSMOP, producing large-scale arrays. Moreover, it is worth noting that the CSMOP workflow was developed with better controlled and more scalable setups and operations compared to existing methods (see **Supplementary Fig. 13** and **Supplementary Note 2** for detailed discussion), demonstrating potential for seamless integration into standard foundry fabrication processes.

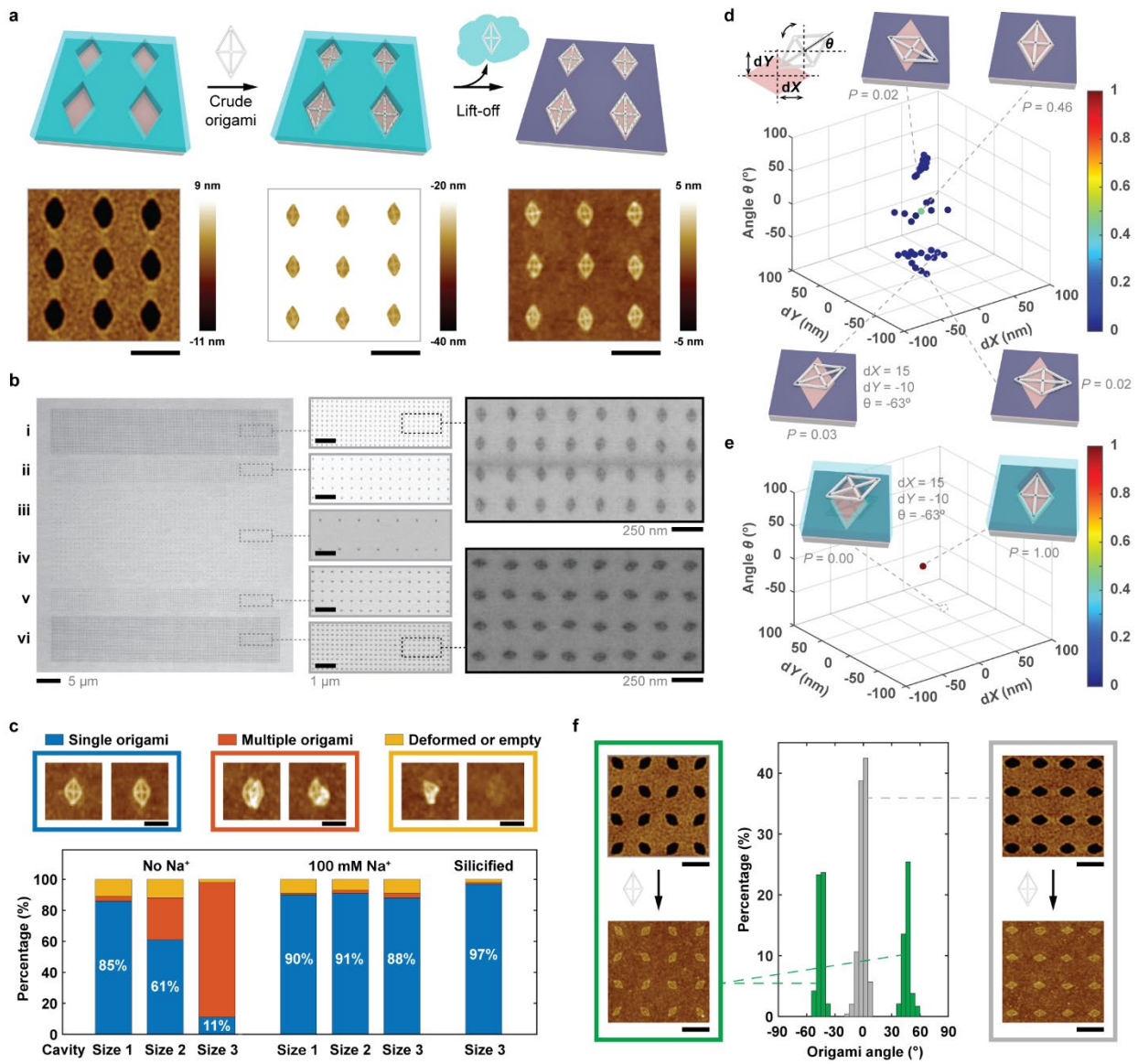

Fig. 2. Cavity-shape modulated placement of 6HB wireframe origami. a, Illustration (top) and AFM images (bottom) of the CSMOP process applied to a rhombic 6HB wireframe origami. Left: rhombic-shaped cavity; middle: rhombic origami placed at the base of the cavity; Right: origami array after resist lift-off. **b**, SEM images of a silicified CSMOP array with rhombic origamis oriented vertically (i, ii, iii) and horizontally (iv, v, vi) and spaced 250 nm (i, vi), 500 nm (ii, v) or 1 μm (iii, iv) apart. **c**, Statistics of CSMOP-directed rhombic origami using increasing cavity sizes (size 1 to 3) with no Na^+ (left), 100 mM Na^+ (middle), or 100 mM Na^+ and silicification (right). Inset: representative AFM images of correctly placed single origami (blue), multiple origamis in one cavity (orange), and deformed origami or an empty cavity (yellow). **d** and **e**, Kinetic modeling prediction of probabilities (P) of origami conformations (dX, dY, θ) from origami placement without (d) or with (e) cavities. Data points representing conformations whose $P = 0$ are omitted. Insets show schematic illustrations of origami conformations. **f**, Rhombic origami orientational distribution and AFM images from CSMOP using a cavity array of 0° (right, grey), and a cavity array of +45° or −45° (left, green) cavity orientations. AFM scale bars: 250 nm for **a**, **f**; 100 nm for **c**.

To better understand how topographical confinement regulated the placement of shape-matched origami, rhombic-shaped cavities of varying sizes were prepared including 97 × 135 nm

(size 1), 106 × 150 nm (size 2), and 114 × 161 nm (size 3), each averaged over 144 cavities measured (sample size $N = 144$) (**Supplementary Fig. 3**). Post-CSMOP analysis revealed that as cavity size increased from size 1 to 2 and then 3, the yield of correctly placed DNA origami monomers decreased from 85% to 61% to 11% ($N = 288$ each), while the occurrence of multiple origami objects positioned within the same cavity rose from 3% to 27% and 86%, respectively (**Fig. 2c**, **Supplementary Fig. 14**). This trend indicated relatively strong origami-substrate interactions under 35 mM Mg^{2+}. Thus, to modulate origami binding kinetics, the deposition solution was modified to include NaCl, as we hypothesized that Na^+ ions would weaken the Mg^{2+}-bridged interactions between the negatively charged DNA origami and the substrate[43, 70-72]. Adding 100 mM Na^+ to the DNA origami placement solution significantly reduced the occurrences of multiple DNA origami binding events, resulting in placement yields of 90%, 91%, and 88% for cavity sizes 1, 2, and 3, respectively ($N = 576$ each), with minimal multiple binding (**Supplementary Fig. 5**). We also hypothesized that the PMMA lift-off process may have removed some origami from the substrate. Indeed, incorporating a silicification step to fix the origami to the substrate prior to removal of the PMMA resist further improved placement yield to 97% ($N = 576$) for cavities of size 3 (**Fig. 2c**, **Supplementary Fig. 15**).

To further elucidate the role of shape-matching cavity confinement, we performed thermodynamic calculations and kinetic simulations to gain insight into the placement process via quantitative modeling (see **Methods**). The rhombic origami placement was modeled both with and without resist cavities, assuming a positive linear relationship between the binding free energy and the overlap in binding area between the origami and the target shape (landing pad or cavity) (**Supplementary Fig. 16**). We calculated the binding free energy of an ensemble of origami-target conformations at distinct translational displacements (dX and dY) between −80 nm and +80 nm using 5 nm increments and rotational displacements (θ) between −90° and +87° in 3° increments, accounting for the rhombic shape's 2-fold rotational symmetry (**Fig. 2d**, top left inset, **Supplementary Fig. 17**). Without cavities, an origami in solution initially diffuses to the flat surface and binds to a silica landing pad and with a randomly positioned and oriented conformation, followed by largely 2D diffusion to maximize their electrostatic surface-binding free energy[52]. After applying a steepest-descent energy minimization mechanism to the set of initial bound conformations, kinetic simulations predicted numerous metastable equilibria or "trapped" end-states away from the correctly positioned and oriented conformation ($dX = dY = 0$, $\theta = 0$) (**Fig. 2d**). Consequently, the probability of correctly placed origami was only ~0.46. In simulating CSMOP, we introduced a free energy penalty associated with bound origami in areas outside of the target shape in order to account for the cavity effect, which was assumed to require a mechanical free energy associated with origami deformation in order to fit in the cavity-confined space while maintaining a specific non-matching conformation (dX, dY, θ) in the ensemble (**Supplementary Fig. 16c** and **Supplementary Note 3**). Conformations with a positive total interaction free energy (binding free energy and free energy penalty combined) were eliminated from the kinetic simulation due to their lack of sufficient binding interaction of origami with the corresponding cavity base to retain them in the well (**Supplementary Fig. 16d**). Consequently, CSMOP simulations demonstrated a single aligned origami conformation ($P = 1.00$) (**Fig. 2e**), owing to the elimination of local free energy minima through topographical cavity confinement. This is consistent with the high placement yield of CSMOP observed experimentally (97%). When a more flexible origami structure was employed, which corresponded to a lower free energy penalty for origami deformation, remaining local free energy minima could still lead to decreased placement yield (**Supplementary Fig. 18** and **Supplementary Note 4**). The free energy penalty correlated

with the mechanical rigidity and deformation response of the origami placed, highlighting the importance of employing mechanically stiff 6HB origami designs. Simulations of the ladder-shaped 6HB wireframe origami (**Supplementary Fig. 19**) and the triangular single-layer origami (**Supplementary Fig. 20**) were also qualitatively consistent with simulation results of the rhombic origami.

Thus, DNA origami orientation could be controlled precisely using EBL-defined cavities. We defined rhombic origami orientation by the orientation of its long-diagonal-axis, between −90° and +90°, consistent with its two-fold rotational symmetry. Using a horizontal rhombic cavity array, 81% of origami monomers oriented horizontally within 0 ± 5° following CSMOP (standard deviation: 4°, N = 245) (**Fig. 2f**, grey; **Supplementary Fig. 14a**). In contrast, a patterned array featuring alternating +45° and −45° rhombic cavities resulted in 86% of origami monomers oriented within either +45° ± 5° or −45° ± 5° (standard deviations: 4° and 3°, respectively, N = 236) (**Fig. 2f**, green; **Supplementary Fig. 21**). This precise spatial and orientational control achieved by CSMOP therefore provides a robust foundation for templating colloidal optical materials for photonic applications and devices.

CSMOP-directed gold NP arrangement

A distinct advantage of CSMOP is its ability to use programmable DNA self-assembly to selectively attach DNA-modified colloidal nanomaterials to the as-deposited origami. While single-particle arrangement of metallic NPs, including gold, has been achieved through lithography-guided placement[34, 65, 73], DNA origami offers unparalleled capabilities to position different NPs at pre-determined sites on a DNA origami with an uncertainty margin down to 1.2 nm[39], facilitating precisely programmed functionalities[38-40]. Previous attempts at deterministic origami-directed gold NP arrangement on surfaces have been limited to AuNSs using the DOP method, typically suffering from NP aggregation and non-specific AuNS adsorption[53, 54]. Moreover, these attempts were restricted to flat, planar substrates, whereas the ability to position colloidal NPs on device architectures with complex topography would significantly enhance their utility. Toward this end, we demonstrate the capability of CSMOP to direct the clean placement of both colloidal AuNSs and AuNRs on EBL-patterned arrays.

To begin, we designed and assembled ladder-shaped 6HB wireframe origami with either a single (**Fig. 3a**, bottom left) or two (**Fig. 3b**, top) binding sites that expressed overhang sequences complementary to DNA strands functionalized on AuNSs. After origami placement and incubation within a AuNS solution, AFM revealed primarily single or paired AuNSs arranged at cavity bases containing origamis with one or two binding sites, respectively (**Fig. 3a**; **Supplementary Figs. 19–20**). While some random AuNS depositions were observed on the resist background (**Supplementary Figs. 22–23**), subsequent PMMA resist lift-off removed them, resulting in clean arrays of origami-directed single AuNSs or AuNS dimers (**Fig. 3a-b**; **Supplementary Figs. 24–25**). We achieved 86% placement yield for single AuNSs and 75% for AuNS dimers (N = 432 each, **Fig. 3c**), surpassing previously reported yields for DOP-directed AuNS placement[54].

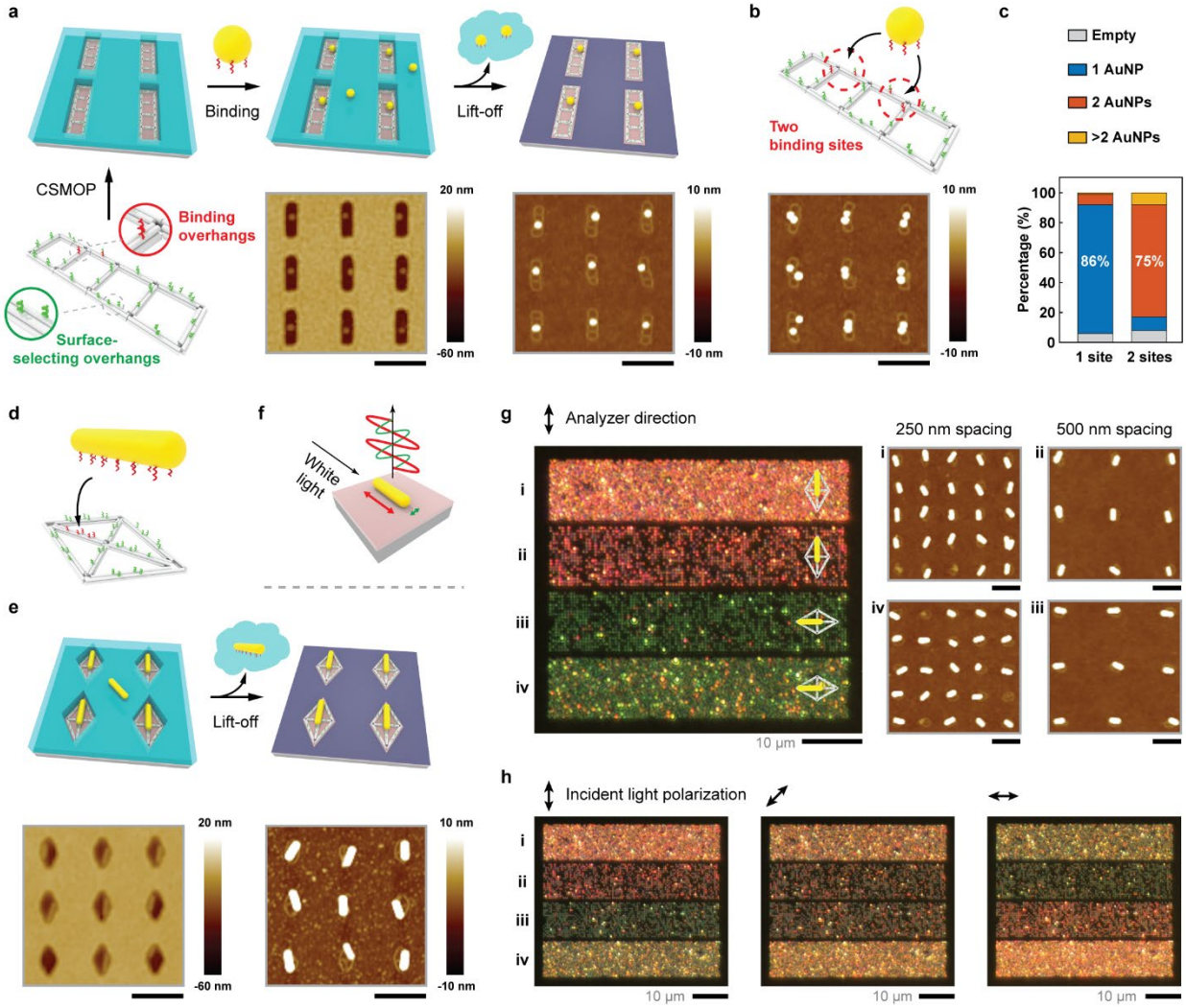

Fig. 3. CSMOP directed AuNS and AuNR arrays. a, Illustrations and AFM images of CSMOP-directed individual AuNS arrangements templated by ladder-shaped origami bearing 1 binding site (3 overhangs). AFM images show organized AuNSs within cavities (middle) and after lift-off (right). **b**, CSMOP-directed arrangement of AuNS dimers with 2 binding sites on origami. **c**, Statistics of AuNS monomers and dimers arranged through CSMOP with origami bearing one or two binding sites. **d**, Illustration of linearly arranged binding overhangs on the rhombic origami for the binding and alignment of AuNRs. **e**, Illustration and AFM images of CSMOP directed AuNR arrangement within the cavity (left) and after lift-off (right). **f**, Illustration of polarization- and wavelength-dependent light scattering from AuNR arrays. **g**, Dark-field microscopy image of CSMOP-directed AuNR arrays with designed vertical (i, ii) or horizontal (iii, iv) orientations and 500 nm (i, iv) or 250 nm (ii, iii) AuNR spacings. Real-color scattered light was observed from unpolarized incident light with a vertically-aligned analyzer. **h**, Dark-field microscopy images of the AuNR array with incident light polarized at 90° (left), 45° (middle) and 0° (right) without an analyzer. All AFM scale bars: 250 nm.

The ability to arrange DNA binding overhangs on origami into customized geometries enables CSMOP to both position and orient anisotropic optical nanomaterials that are valuable in photonic devices. For example, AuNRs have emerged as versatile plasmonic structures for nanophotonics due to their strong, tunable, anisotropic plasmonic properties[74]. Here we demonstrated CSMOP-directed arrangement of AuNRs into arrays with orthogonal orientations by

assembling rhombic origamis with five binding overhangs arranged along the long axis, designed to selectively position and align a single AuNR (**Fig. 3d**). Following DNA origami placement and incubation with DNA-functionalized AuNRs (75 nm × 18 nm), AFM imaging revealed AuNRs assembled on the rhombic origami both before and after the lift-off process, with an individual AuNR placement yield of 68% ($N = 800$) (**Fig. 3e**; **Supplementary Figs. 26–27**). We attribute the deviation from ideal AuNR alignment to capillary force-driven reconfiguration during the drying process. Specifically, the movement of the drying water meniscus drags the AuNRs at the water-air interface towards the sidewalls of the cavity (**Supplementary Fig. 28** and **Supplementary Note 5**). This hypothesis is supported by the observation that most AuNRs are positioned against cavity walls rather than at cavity centers after drying.

Because plasmonic light scattering of AuNRs depends on both wavelength and the relative angle between incident light polarization and AuNR orientation, we predicted that CSMOP could prepare substrates with anisotropic light scattering response by aligning arrays of AuNRs in different orientations[75-77] (**Fig. 3f**). We therefore fabricated a 5 μm × 4.5 μm AuNR array comprising four 5 μm × 1 μm array strips containing rhombic origamis oriented vertically or horizontally with 250 nm or 500 nm spacings (**Fig. 3g**; **Supplementary Figs. 27, 29**). Under unpolarized incident light in dark-field microscopy, vertically aligned AuNRs (i and ii) primarily scattered red light along the vertical direction (analyzer direction) arising from longitudinal plasmon resonance, while horizontally aligned AuNRs scattered primarily green light from transverse plasmon resonance (**Fig. 3g**). Similarly, under polarized incident light (without an analyzer), AuNR arrays appeared as red, green, or a mixture depending on their orientation relative to the polarization of the incident light (**Fig. 3h**). Using this method, we created a pattern of the MIT logo with dynamic tunable coloration (**Supplementary Fig. 30**). Thus, the ability of CSMOP to exploit anisotropic plasmonic properties of AuNRs shows promising potential for applications in metasurfaces[78, 79] and optical data storage[80, 81].

CSMOP-directed QR arrangement

Colloidal QDs and QRs have well-engineered scalable syntheses and near-unity tunable photoluminescence (PL) and electronic properties, making them attractive for electronics[82], light-emitting devices[83] and quantum information science[84]. QRs, in particular, offer unique opportunities to engineer efficient coupling with photonic devices due to their morphology-dependent emission polarization[85-88]. However, methods for the deterministic integration of individual colloidal QRs using origami templates face the challenge of colloidal metastability[43], because DNA-functionalized QRs typically aggregate under high Mg^{2+} concentrations required for origami placement. While previous research has shown that origami-substrate attachment under Mg^{2+}-free environments can be stabilized using carefully designed crosslinking reactions between the substrate and amine-modified DNA origamis[50], the integrity and accessibility of DNA hybridization following such chemical reactions have yet to be demonstrated. Here, we instead introduce a straightforward and versatile soft-silicification-passivation method to enhance the robustness and attachment of the origami templates under Mg^{2+}-free conditions, thereby enabling the application of CSMOP to colloidal nanomaterials that are typically unstable in the presence of divalent cations (**Fig. 4a**).

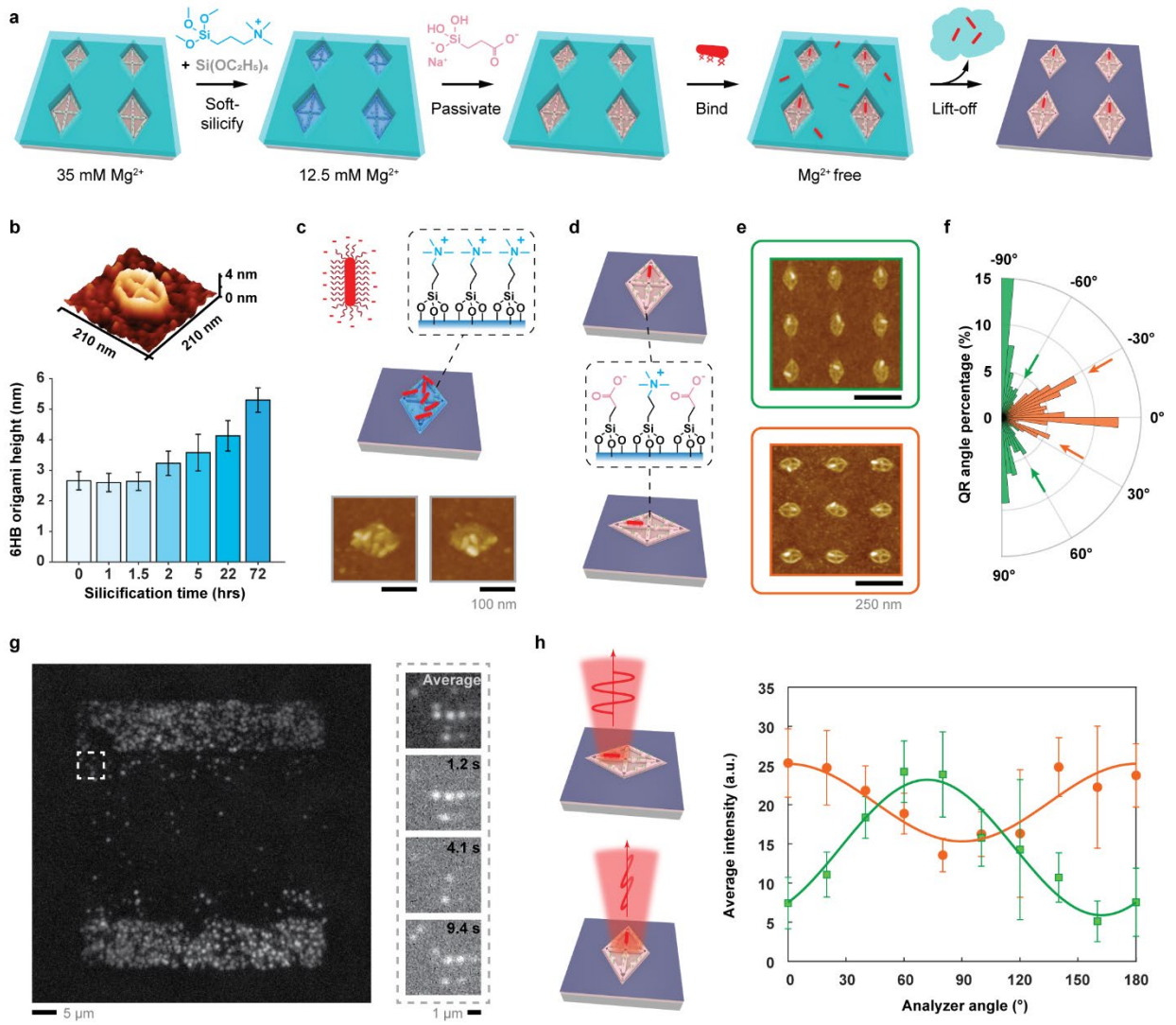

Fig. 4. Soft-silicification-passivation enabled CSMOP-directed QR array. a, Schematic illustration of the workflow: CSMOP array soft-silicification, passivation, QR binding, and lift-off. **b**, Dry AFM origami height with increasing silicification time. Inset: 3D height profile of a rhombic origami after 1.5 h silicification. **c**, Illustration and AFM images of random QR attachment onto silicified CSMOP origami via electrostatic interactions. **d**, Illustration of surface charge change after passivation on origamis with orthogonal orientations. **e**, AFM images of CSMOP directed individual QR binding to vertically (top, green) and horizontally (bottom, orange) aligned origamis. **f**, Orientation distribution of QRs directed by vertical (green) and horizontal (orange) CSMOP origamis. Arrows highlight major orientation deviations from design. Inset: example of a misaligned QR configuration trapped by the wireframe structure. **g**, Widefield PL image of a CSMOP directed QR array (maxima-projected image of 100 frames over 10s). Inset: zoomed-in image of the QR array at different time points and the averaged image (top). Frame exposure time: 100 ms. **h**, Averaged PL intensity as a function of the analyzer angle from vertically (green) and horizontally (orange) aligned QR arrays.

Specifically, we carefully silicified the CSMOP-directed origami within cavities, adapting existing DNA origami silicification techniques[89, 90], in order to secure origami attachment to the substrate without compromising the binding availability and affinity of protruding single-stranded DNA overhangs. Dry AFM imaging revealed that origami height remained stable at around 2.6 nm

after up to 1.5 h of silicification, then increased to 5.3 ± 0.4 nm over 72 h (**Fig. 4b**; **Supplementary Fig. 31**), indicating origami structure rigidification via silica deposition. We found that as short as a 1.5-hour silicification time ensured stable origami attachment to the substrate under Mg^{2+}-free conditions (termed soft-silicification, compared to days of silicification in previous work[50, 53]). However, direct QR incubation with silicified DNA origami resulted in random QR attachment, likely because DNA silicification created positively charged silica surfaces that resulted in non-specific electrostatic attractions between the DNA-modified QRs and the silicified origami (**Fig. 4c**; **Supplementary Fig. 32**). To address this, we passivated the silica surfaces with negatively charged silane (see **Methods**). The resulting negatively charged silica surfaces promoted QR binding exclusively through designed sequence-dependent DNA hybridization (**Fig. 4d**). Consequently, we observed individual QRs attached at each CSMOP origami position with 79% yield of single QR placement (N = 720) (**Fig. 4e**; **Supplementary Figs. 33–34**). Orientational analysis revealed that 73% single QRs oriented within 90 ± 30° with vertical CSMOP template (N = 346) (**Fig. 4f**, green; **Supplementary Fig. 33**), while 67% of single QRs exhibited 0 ± 30° orientation after horizontal CSMOP (N = 326) (**Fig. 4f**, orange; **Supplementary Fig. 34**). Notably, we also observed clusters of QR orientations deviating by around ±30° from the designed orientation (**Fig. 4f**, arrows), which may be attributable to the capillary force-driven reconfigurations discussed above (**Supplementary Fig. 35**). While hybridization of ssDNA to silicified origami has been demonstrated[91], our work is the first we are aware of that shows programmable binding of DNA-functionalized NPs post-silicification. Because colloidal nanomaterials functionalized with numerous DNA strands are more prone to steric hindrance and non-specific aggregation than individual oligonucleotides, our soft-silicification strategy provides an important step in preserving binding overhang accessibility for larger NPs and subsequent passivation in preventing random electrostatic interactions.

Using this new protocol, we fabricated QR arrays with QR position and alignment controlled by CSMOP origami array templates to establish a foundation to mimic functional optical devices. Widefield fluorescence microscopy revealed QR PL emission from individual QRs in the array under 532 nm excitation (**Fig. 4g**). We observed strong stochastic PL intermittency (*i.e.*, blinking) and non-radiative QR populations (**Fig. 4g**, inset; and **Supplementary Video 1**). QD blinking and non-radiative states are ubiquitous phenomena often associated with surface traps and charging-induced Auger recombination[92, 93], which can be mitigated through QD surface passivation[94, 95] or external optical manipulation[96]. To demonstrate deterministic CSMOP-enabled emission polarization control of the QR arrays, we monitored average emission intensity as a function of analyzer angle from the two QR arrays templated by CSMOP origamis with orthogonal orientations (**Supplementary Fig. 36**). Results showed sinusoidal relationships between PL intensity and analyzer angle for both arrays, with roughly anti-correlated PL intensity (**Fig. 4h**), indicating ensemble alignment of QRs in respective arrays with roughly orthogonal orientations. The offset between the maximum and the minimum of the two QR array intensities, respectively, was attributed primarily to the sizeable QR orientation outliers around ± 30° discussed above. Notwithstanding, to our knowledge this represents the first demonstration of controlling polarized emission from individual colloidal emitters by deterministic engineering of emitter configuration on device substrates, much less using a scalable, bottom-up fabrication approach.

CSMOP-directed deterministic QR integration with silicon photonics

Integrating colloidal quantum emitters within practical devices typically requires the particles to be placed on non-uniform topographies[15-18]. CSMOP provides a significant advantage in this regard, as the presence of the cavity resist layer prevents non-specific adsorption to the sidewalls of such structures. To demonstrate deterministic integration of individual colloidal quantum emitters within silicon photonics using CSMOP, we fabricated chips with 310 nm high SiN_x photonic structures on a 3 μm silica layer on silicon substrate, including slab waveguides, micro-ring resonators, and bullseye cavities (**Fig. 5**; **Supplementary Fig. 37**; see **Methods** for fabrication process). We first evaluated CSMOP on simple slab waveguides, a fundamental building block of PICs (**Fig. 5a**). Specifically, SiN_x structures were treated with O_2 plasma to create surface silanol groups. After PMMA coating, cavities orthogonal or parallel to the waveguide were fabricated on the slab surface using EBL (**Fig. 5b**), with cavity depths of 46 nm, 62 nm, or 86 nm for waveguides of 0.5 μm, 1 μm, and 2 μm, respectively, due to topographically affected spin coating of the resist (**Supplementary Fig. 38**). After CSMOP, we observed a high origami placement yield of 94% (N = 336) on 2 μm SiN_x slab waveguides, despite a deeper cavity depth (86 nm) than that on a flat substrate (~30 nm) (**Supplementary Fig. 39**). Subsequent QR incorporation created deterministically placed individual QRs directed by CSMOP on SiN_x waveguides with a 43% (N = 329) placement yield of individual QRs (**Fig. 5c**; **Supplementary Fig. 40**).

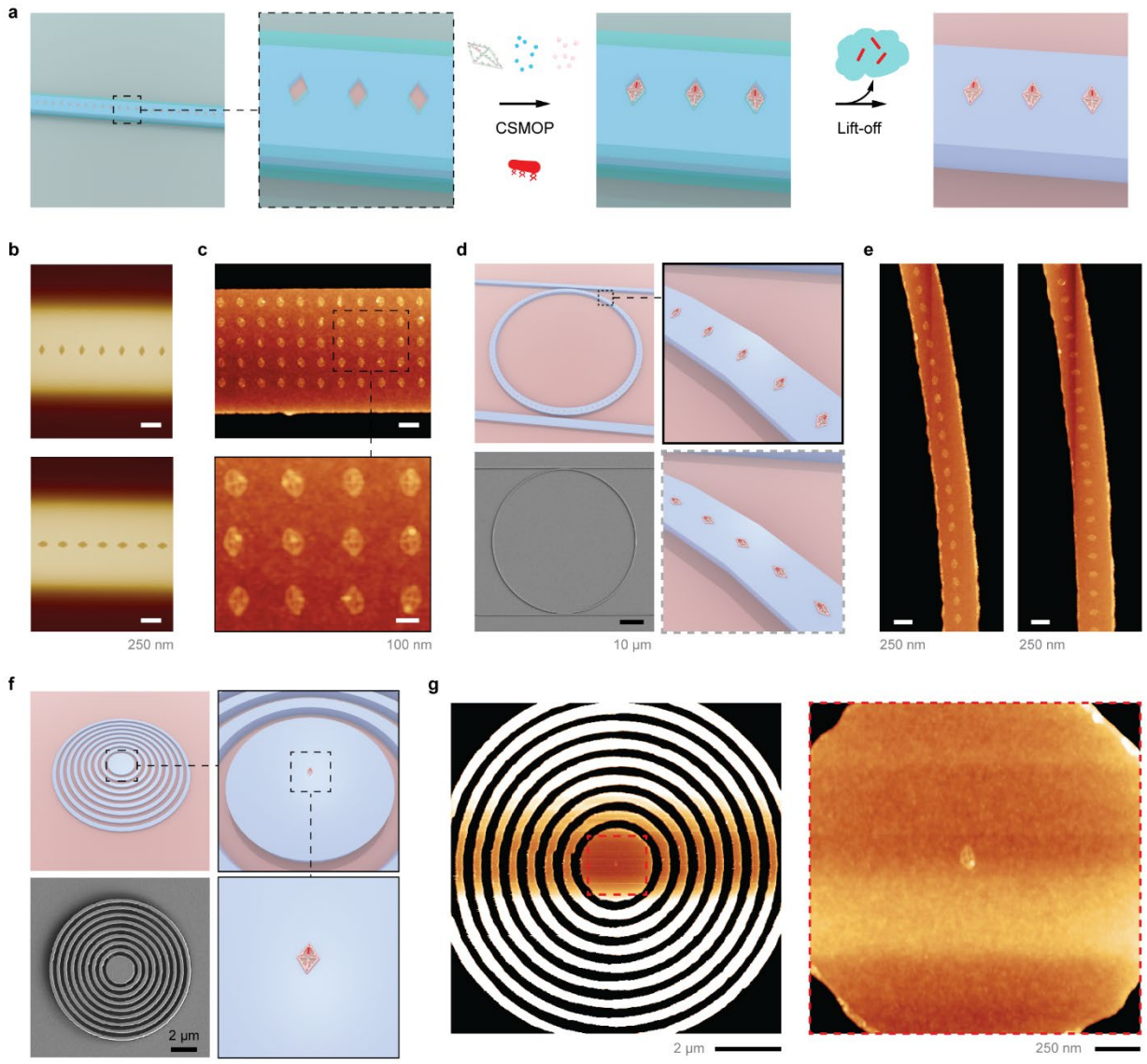

Fig. 5. CSMOP-directed deterministic QR integration with photonic structures. a, Schematic illustration of the CSMOP-directed QR placement on SiN_x waveguide with an orthogonal orientation. Trimethoxysilyl coating and oxidation layers are omitted. **b**, AFM images of orthogonal and parallel PMMA cavities on 1 μm slab waveguides. **c**, AFM images of CSMOP-directed QRs on a 2 μm slab waveguide. **d**, Illustration of CSMOP-directed QRs on a micro-ring resonator, and an SEM image of the micro-ring structure (bottom left). **e**, AFM images of CSMOP-directed QRs on micro-ring structures with a parallel (left) or orthogonal (right) orientation. **f**, Illustration of a single CSMOP-directed QR at the center of a bullseye cavity, and an SEM image of the bullseye cavity (bottom left). **g**, AFM images of a single CSMOP-directed QRs at the center of a bullseye cavity.

Because integrating colloidal QDs with micro-ring resonators has potential applications in lasers[97] and optical sensors[98], we demonstrated deterministic CSMOP-directed QR placement on a SiN_x micro-ring structure with a width of 0.45 μm (**Fig. 5d** and **5e**; **Supplementary Fig. 41**). QR orientation was engineered to be perpendicular or parallel to the tangential direction of the ring. Additionally, bullseye cavities are promising photonic structures to enhance emission for quantum optics[99], but a key challenge is positioning the emitter at the cavity center to avoid

artificial defects, such as uncontrolled emission polarization[100]. Thus, next we harnessed the capability of CSMOP to deterministically place a single QR at the center of a bullseye cavity (**Fig. 5f** and **5g**; **Supplementary Fig. 42**) with a device fabrication yield of 49% (18 out of 37 bullseye structures imaged), offering potential applications in quantum optics. In particular, future work will investigate the material and design of both the photonic structures and the colloidal QDs towards fabrication of single-photon sources for potential quantum computing PICs (**Supplementary Note 6**). Importantly, we note that DNA origami placement is compatible with various optical device materials, including diamond-like carbon[49], glass[60], TiO_2[101], and semiconductor 2D materials like graphene[102, 103] and transition metal dichalcogenides[104]. This versatility extends the breadth of potential applications of CSMOP well beyond silicon-based photonics alone[3, 105].

Conclusions

We developed a cavity-shape modulated origami placement method, effectively bridging bottom-up molecular and colloidal synthesis with top-down fabrication of complex photonic devices. Combining DNA origami with electron beam lithography-defined cavities, we achieved precise control over the integration of nanoscale optical materials with micron-sized photonic structures. The versatility of CSMOP was demonstrated by the successful arrangement of AuNS arrays with high yield and controlled orientation of anisotropic AuNRs, advancing numerous possibilities for nanoplasmonics. In a significant advance, our soft-silicification-passivation strategy overcame the challenge of integrating metastable colloidal QRs within photonic structures, ensuring stable origami templating while maintaining DNA hybridization capabilities. This development enabled deterministic positioning of individual quantum emitters within complex photonic architectures, as demonstrated by our successful integration of QRs with silicon nitride waveguides, micro-ring resonators, and bullseye cavities. CSMOP offers several important advantages over existing techniques, providing nanometer-scale control, scalability of fabrication, broad compatibility across various nanomaterials and photonic device architectures, and therefore potential for large-scale integration. Its built-in lift-off process ensures clean device surfaces with minimal-to-no background, and its compatibility with standard foundry fabrication processes offers promising potential for industrial implementation. As research in quantum information science and nanophotonics advances, CSMOP serves as an effective platform for the integration of quantum emitters and other nanoscale optical materials. By enabling deterministic placement of colloidal nanomaterials within photonic integrated circuits, this work therefore provides a foundation for developing sophisticated quantum photonic devices, contributing significantly to progress in valuable quantum technologies and related fields.

Methods

DNA origami design and assembly

6HB wireframe origamis were designed using ATHENA[106]. Design details and DNA sequences are provided in **Supplementary Note 1**. Origamis were folded using a reported method[107] in a 12.5 mM $MgCl_2$ buffer containing 40 mM Tris (tris(hydroxymethyl)aminomethane) and 12.5 mM $MgCl_2$ (pH = 8.0 ± 0.2). Specifically, 2 nM DNA scaffold (M13mp18/p7249, Tilibit nanosystems)

was mixed with 20 equivalent unmodified staple strands and 60 equivalent modified staple strands (with binding sequences) (standard desalting, Integrated DNA Technologies (IDT)) in 12.5 mM $MgCl_2$ buffer. The mixed solution was annealed in a thermocycler (Biorad T100) using the following program: 95 °C for 5 min, 85 °C to 76 °C at 5 min/°C, 75 °C to 30 °C at 13.75 min / 0.5 °C, 29 °C to 25 °C at 10 min/°C, then held at room temperature (*ca.* 23 °C). The folded origami sample was used directly for CSMOP without further purification to remove excess staple strands.

DNA functionalization of NPs

A thiolated ssDNA was used to functionalize all NPs in this work. The ssDNA was purchased as a disulfide-modified DNA strand from IDT with standard desalting (sequence: /5ThioMC6-D/TTTTTTTTTCCCAGGTTCTCT), and reduced by 100 equivalent Tris(2-carboxyethyl)phosphine hydrochloride (TCEP) at a final concentration of 1 mM.

DNA functionalization of AuNSs was performed using a previously reported freezing-assisted method[108]. Citrate-stabilized AuNS (17 nm diameter) was synthesized following a standard seeded growth protocol[109]. A volume of 1 mL synthesized AuNS (2 nM) was mixed with 6000 equivalent thiolated DNA and kept in a −80 °C freezer for 15 min, followed by defrosting at room temperature. The completely thawed solution was then washed six times with 10 mM NaCl buffer (10 mM Tris, 10 mM NaCl, pH = 8.0 ± 0.2) by centrifugation at 16000 rcf for 3 min. Purified DNA-functionalized AuNS solution was quantified by UV-vis absorption at 450 nm (extinction coefficient: 324000000 $M^{-1}cm^{-1}$).

DNA functionalization of AuNRs was performed using a previously reported dehydration-assisted method[110]. A volume of 2 mL of 0.1 nM citrate-stabilized AuNR (nanoComposix, catalog number: GRCN800) was pelleted by centrifugation at 6000 rcf for 5min. After removing the supernatant, 30000 equivalent thiolated DNA was added, with a final volume of around 20 µL. After thorough mixing of the DNA and AuNR, 180 µL 1-butanol was added, followed by brief vortex mixing. A volume of 200 µL 10 mM NaCl buffer was then added to the mixture followed by another quick vortex mixing and brief centrifugation at 2000 rcf for several seconds to facilitate liquid phase separation, with DNA-functionalized AuNRs dispersed in the bottom aqueous phase. The aqueous phase was collected and the dispersed DNA-functionalized AuNRs were washed six times with 10 mM NaCl buffer by centrifugation at 4000 rcf for 4 min. Purified DNA-functionalized AuNR solution was quantified by UV-vis absorption at 830 nm (extinction coefficient: 5900000000 $M^{-1}cm^{-1}$).

DNA functionalization of QRs was performed using a previously reported ultrasonication-dehydration-assisted method[43]. A volume of 10 µL of 5 mg/mL CdSe/CdS core-shell type QRs in hexane (Sigma, catalog number: 900514) was mixed with thiolated ssDNA at a molar ratio of 500:1 (DNA:QR) in the presence of 100 mM NaOH to reach a final volume of around 50 µL. The mixture was sonicated at 37 kHz for 5 min, immediately followed by the addition of 600 µL 1-butanol and brief vortex mixing. Subsequently, 200 µL 10 mM NaCl buffer was added to the mixture followed by another quick vortex and brief centrifugation at 2000 rcf for several seconds to facilitate liquid phase separation, with DNA-functionalized QRs dispersed in the bottom aqueous phase. The aqueous phase was collected and the dispersed DNA-functionalized QRs were purified and concentrated using an ultracentrifugal filter (Amicon 100 kDa) six times (8000 rcf for 3 min each time). Purified DNA-functionalized QR solution was quantified by UV-vis absorption at 350 nm (extinction coefficient: 64850000 $M^{-1}cm^{-1}$).

SiN_x photonic structure chip fabrication

The fabrication of the chips started with a 100 mm Si (100) wafer (p-type Boron-doped) with 3 µm of thermally grown wet oxide (prime grade, University Wafer Inc.). Upon receipt, the wafer was thoroughly cleaned following the RCA clean protocol. The process consisted of two sequential cleaning steps: RCA-1 (7:2:2 mixture of DI water : ammonium hydroxide : hydrogen peroxide) followed by RCA-2 (7:2:2 mixture of DI water : hydrochloric acid : hydrogen peroxide). For each step, the solution was heated to 75 °C and the wafer was cleaned for 10 min, followed by DI water rinse. After the complete RCA clean, the wafer was dried using a spin rinse dryer. After rinsing in deionized water and drying using a spin rinse dryer, the wafers were loaded in a Low-Pressure Chemical Vapor Deposition Chamber (Tystar Mini Tytan 4600) to deposit the SiN_x layer. The SiN_x deposition was performed at 770 °C, with a pressure of 250 mTorr, 25 sccm of dichlorosilane and 75 sccm of ammonia, resulting in a growth rate of *ca.* 3.41 nm/min. A thickness of 310 nm was targeted for the SiN_x film. After the growth, the refractive index and thickness of the film were characterized with reflectometry (Filmetrics F50) and ellipsometry (J.A. Woolam model RC2), followed by singulation of the wafer into individual pieces through cleaving.

To pattern the waveguides, the chips were first coated with an adhesion promoter hexamethyldisilazane (HMDS) at 150 °C in a YES-310TA vapor prime oven for 1 min (Yield Engineering Systems Inc). A thin UV-sensitive negative photoresist (AZ-nLOF 2020, Microchemicals GmbH) was coated onto the chips using a CEE Apogee Spin coater with a spin speed of 2000 rpm for 60 s, followed by baking at 110 °C for 1 min. Before spinning, the photoresist was first diluted in an equal amount by volume of methyl isobutyl ketone to achieve a lower thickness on the chip, more suitable to achieve high lithographic resolution. The chips were subsequently coated with a thin conductive layer (ESpacer 300Z from Resonac) by spin coating at 4000 rpm for 45 s. Exposure of the resist was performed using an ELS-BODEN electron beam lithography system (Elionix HS-50), with an operating current of 10 nA and beam voltage of 50 keV. After exposure, the chips were rinsed in water to remove the conductive layer, post exposure baked at 115 °C for 1 min, developed in a 2.38% TMAH-based developer (AZ 726) for 2 min, and thoroughly rinsed with deionized water. Subsequently, the patterned chips were dry etched using an Inductively Coupled Plasma Reactive Ion Etcher (Samco RIE-230iP) at a pressure of 1 Pa, 300 W ICP power, 100 W bias power, 20 sccm of CF4 and 60 sccm of Ar. After etching, the photoresist mask was stripped using an O_2 plasma (ESI 3511V-001).

Fabrication of resist cavity on silicon chips

Cavities in the resist layer were fabricated using a standard EBL process. Silicon chips (1 cm × 1 cm) cleaved from a 100 mm Si (100) wafer (p-type Boron-doped) with a 90 nm dry thermal oxide (prime grade, University Wafer Inc.) were first cleaned by ultrasonication in isopropanol (IPA) for 10 min and dried with pressurized N_2, followed by O_2 plasma treatment at 500 W, 255 duty ratio with 10 sccm O_2 for 2 min on a Tergeo Plus Plasma Cleaner (PIE Scientific LLC). The chips were then primed with HMDS at 150 °C in a YES-310TA vapor prime oven for 1 min (Yield Engineering Systems Inc). PMMA resist (950 A2 in anisole, MicroChem) was spin coated on the chips at 4500 rpm for 1 min and baked at 180 °C for 5 min, yielding around 60 nm thick resist layer. Next, EBL was performed to expose the PMMA coated chips with various doses for origami-shaped patterns using an ELS-BODEN system (Elionix HS-50) with an operating current of 2 nA and beam voltage of 50 keV. The target pattern dimensions were 150 nm × 80 nm (long and short axes length) for the rhombic structure, 150 nm × 40 nm (length and width) for the ladder-shaped structure, and 145

nm (edge length) for the equilateral triangular structure. Proximity Effect Correction (PEC) was applied with the BEAMER software when feature spacing was 250 nm. The exposed patterns were developed with MIBK/IPA 1:3 (MicroChem) at 4 °C for 50 s to reveal the cavities, rinsed with IPA, and dried with pressurized N_2. Developed patterns were then exposed to directional O_2 plasma on a RIE-230iPC system (SAMCO) for 18 s at 20 °C, 2.7 Pa with 50 W bias and 20 sccm O_2 to oxidize the cavity base surface. Cavity depth (*i.e.* PMMA resist layer thickness) was measured to be around 30 nm after the RIE O_2 plasma treatment. Increasing EBL doses from 1020 μC/cm^2 to 1320 μC/cm^2 and 1722 μC/cm^2 resulted in 97 × 135 nm (size 1), 106 × 150 nm (size 2), and 114 × 161 nm (size 3) as the short and long axes length of the rhombic cavity openings measured by AFM, respectively. Note that AFM measurements were convoluted with probe size and imaging parameters, and O_2 plasma etching expanded the cavity opening, both with potential bias on sharp cavity vertices.

In a typical practice, two copies of the same pattern were fabricated on the two halves of the 1 cm × 1 cm chip and cleaved into two 0.5 cm × 1 cm chips using a PELCO LatticeAx 420 system (Ted Pella Inc) for the downstream origami placement. For chips fabricated with SiN_x photonic structures (1 cm × 1 cm), the resist cavity fabrication process remained the same except that 950 PMMA A4 was employed for coating and baking, followed by spin coating of DisCharge H_2O (4×, DisChem Inc) to improve electron conductivity. After aligned EBL exposure with global fiducial markers, the chips were first rinsed with water to remove the DisCharge coating, then developed using the same method for 90 s. As fabricated cavities on the SiN_x structure exhibited varied cavity depths depending on the SiN_x structure dimensions, due to spin coating on topographical substrates.

Cavity modulated origami placement

In a typical CSMOP process, crude DNA origami directly from folding at 2 nM in 12.5 mM $MgCl_2$ buffer was first diluted and adjusted to 1 nM with a final $MgCl_2$ concentration of 35 mM and NaCl concentration of 100 mM. A volume of 20 μL crude origami solution was pipetted onto a 0.5 cm × 1 cm silicon chip bearing EBL-fabricated cavity patterns. The chip with origami solution was incubated at room temperature (23 °C) for 2 h in a large petri dish lined with wet Kimwipes (Kimtech) to reduce evaporation, with gentle shaking at 300 rpm on a plate shaker (BioShake iQ). After incubation, the chip was transferred into a well filled with 0.9 mL 40 mM $MgCl_2$ buffer (containing 10 mM Tris and 40 mM $MgCl_2$, pH = 8.0 ± 0.2) on a 48-well culture plate (10861-560, VWR), with the patterned side facing up. The chip was washed by shaking the plate at 700 rpm for 5 min and then transferred into another well with 0.9 mL fresh buffer for the next wash. All chip washing steps in this research were performed this way by shaking the well plate with chip in a well containing the wash buffer. In total, the chip was washed 4 times in 0.9 mL 40 mM $MgCl_2$ buffer and 2 more times in 0.9 mL 60 mM $MgCl_2$ buffer (containing 10 mM Tris and 60 mM $MgCl_2$, pH = 9.0 ± 0.2) to remove excess DNA origami and staple strands while enhancing substrate binding with higher Mg^{2+} concentration and higher buffer pH. The chip was then dried by first quickly dipping in water twice to remove bulk residual buffer and blow-dried with pressurized air. To remove the PMMA layer (*i.e.* lift-off), the dried chip was placed in a *N*-methylpyrrolidone (NMP) bath and ultrasonicated at Power 0 for 6 min using a sweepSONIK (40 kHz dualSWEEP) ultrasonic generator (Blackstone-NEY Ultrasonics, Cleaning Technologies Group, LLC). The chip was then transferred to and stirred for 1 min in an acetone bath and IPA bath consecutively and dried with pressurized N_2.

For the CSMOP process on a chip with SiN_x photonic structures (1 cm × 1 cm), 100 µL origami solution was applied and incubated with the chip for 3 h. The chip was washed in a 24-well culture plate (10861-558, VWR) with 2 mL wash buffers each time to adapt for the larger chip size.

To silicify the placed DNA origami for SEM characterization (not a soft-silicification, see below), a silicification precursor solution was prepared freshly by adding 75 µL (3-aminopropyl)triethoxysilane (APTES, 99%, 919-30-2, Sigma-Aldrich) and 150 µL tetraethyl orthosilicate (TEOS, ≥ 99% GC, 78-10-4, Sigma-Aldrich) to 4.775 mL 12.5 mM $MgCl_2$ buffer sequentially with vortex mixing in between. The mixture was incubated at room temperature with 900 rpm shaking for 30 min and left undisturbed for 20 min, followed by filtration through a 0.22 µm centrifuge tube filter (Corning Costar Spin-X). After CSMOP, prior to drying, the origami-placed chip was transferred to a new well containing 1 mL as prepared silicification precursor solution, and incubated for 1.5 h with 500 rpm shaking. The chip was then washed in 0.9 mL 12.5 mM $MgCl_2$ buffer 4 times in the plate well. Drying and lift-off processes were performed as described above.

CSMOP directed gold NP arrangement

To guide the gold NP arrangement on silicon chip, DNA origami with binding overhangs was first placed through CSMOP as described above until after the 40 mM $MgCl_2$ buffer washes. The chip was removed from the buffer solution and its back side dried with a Kimwipe, without removing the liquid on the top side of the chip. The chip was placed back into the humid petri dish and 20 µL of 10 nM DNA functionalized AuNSs (or 1 nM DNA functionalized AuNR) in 40 mM $MgCl_2$ buffer was added to the liquid on the top surface of the chip. After pipetting the liquid in and out 10 times for mixing, the chip was incubated in the petri dish at room temperature for 4 h (2.5 h for AuNR). The chip was then washed 4 times in 0.9 mL 40 mM $MgCl_2$ buffer and 2 times in 0.9 mL 60 mM $MgCl_2$ buffer in the plate to remove excess AuNSs. Drying and lift-off processes were performed as described above.

CSMOP directed QR arrangement

To guide the QR arrangement on silicon chip, DNA origami with binding overhangs was first placed through CSMOP and then soft-silicified to adapt to a Mg^{2+}-free condition. A soft-silicification precursor solution was prepared freshly by adding 150 µL N-trimethoxysilylpropyl-N,N,N-trimethylammonium chloride (TMAPS, 50% in methanol, 35141-36-7, Fisher Scientific) and 150 µL TEOS, to 4.7 mL 12.5 mM $MgCl_2$ buffer sequentially with vortex mixing in between. The mixture was incubated at room temperature with 900 rpm shaking for 30 min and left undisturbed for 20 min to allow large silica particles formed to float to the top of the solution. A 1 mL volume of as prepared soft-silicification solution was taken from the bottom of the mixture (avoiding large particles at the top) and added to a well on the 48-well plate. After origami placement in the CSMOP process, the chip was washed 3 times in 0.9 mL 40 mM $MgCl_2$ buffer and once in 0.9 mL 60 mM $MgCl_2$ buffer on the plate, before transferred to the well containing the soft-silicification precursor and incubated for 1.5 h. After soft-silicification, the chip was washed 4 times with 0.9 mL 12.5 mM $MgCl_2$ buffer and transferred to another well containing 1 mL passivation solution. The passivation solution was freshly prepared by mixing 200 µL carboxyethylsilanetriol disodium salt (CTES, 25% in water, 18191-40-7, Oakwood) with 4.8 mL 12.5 mM $MgCl_2$ buffer and 30 µL concentrated hydrochloric acid (37%, 7647-01-0, Sigma-Aldrich) and filtered through an Amicon Ultra Centrifugal Filter (10 kDa, Sigma). The chip was incubated

in the passivation solution for 15 min, followed by 2 washes in 0.9 mL 12.5 mM $MgCl_2$ buffer and 3 washes in 0.9 mL PBS buffer (without calcium and magnesium, pH = 7.4 ± 0.1, 21-040, Corning).

After passivation, the chip was removed from the buffer solution and its back side dried with a Kimwipe, without removing the liquid on the top side of the chip. The chip was placed back into the humid petri dish and 20 μL of 20 nM DNA functionalized QRs in PBS buffer was added to the liquid on the top surface of the chip. After pipetting the liquid in and out 10 times for mixing, the chip was incubated in the petri dish at room temperature for 4 h. The chip was then washed 4 times in 0.9 mL PBS buffer and 2 times in 0.9 mL 60 mM $MgCl_2$ buffer in the plate to remove excess QRs. Drying and lift-off processes were performed as described above.

For CSMOP directed QR placement on a chip with SiN_x photonic structures (1 cm × 1 cm), the chip was soft-silicified, passivated, and washed in a 24-well culture plate (10861-558, VWR) with 2 mL corresponding solution to adjust for the larger chip size. A volume of 100 μL QR solution was applied and incubated with the chip for QR binding.

Kinetic simulation

The two-dimensional projected DNA structures and corresponding deposition shapes were illustrated with consideration of their nanoscale dimensions: 125 nm × 75 nm for the rhombic structure, 140 nm × 40 nm for the ladder-shaped structure, and 140 nm × 120 nm for the triangular structure.

To calculate the thermodynamic energy landscapes, we established a conformational grid on the x and y coordinates, along with the angle θ (representing the rotation of a structure relative to its deposition shape about the principal axis). Using each deposition location as the origin, grid points were defined as: $-80\text{ nm} \leq X \leq 80\text{ nm}$ and $-80\text{ nm} \leq Y \leq 80\text{ nm}$ with 5 nm intervals, and $-90° \leq \theta \leq 90°$ for rhombic and ladder-shaped structures and $-60° \leq \theta \leq 60°$ for triangular structure with 3° intervals. For each grid point, we calculated the overlapped area (A_o) between a structure and its deposition shape by generating alpha shapes and summing triangulated overlapped regions. The binding free energy for both non-cavity and cavity cases was determined as $E_b = u_b A_o$, where u_b is the assumed binding free energy per area (−0.001). The free energy penalty, calculated only for the cavity case, was set as $E_r = u_r A_r$, where u_r is the assumed free energy penalty per area (0.001α, with α as the free energy penalty coefficient) and A_r is the remaining area (area outside of the cavity). The total interaction free energy was computed as $E = E_b + E_r$.

For kinetic simulations, we assumed each grid point as an initial conformation and allowed the DNA structure to move toward more energetically favorable conformations. The perturbing intervals for searching neighboring conformations were set to ± 5 nm for X and Y positions, and ± 3° for rotation angle θ. From each initial conformation, the DNA structure was translated or rotated to the neighboring conformation with the lowest total interaction free energy (E) of its 6 neighbors until reaching a local free energy minimum. In the case of origami-cavity simulations, initial conformations with a positive total interaction free energy (E) were eliminated due to the lack of origami interaction with the cavity base (See **Supplementary Note 3-4**).

AFM and SEM characterization

AFM measurements were performed under air conditions using an Asylum Research Jupiter XR AFM (Oxford Instrument) in tapping mode. Measurements employed 55AC-NG gold-coated ultra-high frequency AFM probes (tip radius < 7 nm, f_o = 1200 kHz; 85 N/m, NanoAndMore).

SEM measurements were conducted using a Zeiss Sigma HD VP Scanning Electron Microscope operating at 2 kV. Silicified CSMOP DNA origami arrays on silicon chips were imaged using an Inlens Secondary Electron Detector without coating. Images of SiN_x photonic structures were taken using an Everhart Thornley Secondary Electron Detector after gold coating using a PELCO SC-7 Sputter Coater for a 5-second autocycle.

Optical microscopy

Dark field microscopy of CSMOP directed AuNR arrays was performed using a Nikon Eclipse LV150NA microscope with a DS-Ri2 camera and a 100× air objective (Nikon MUE61900 EPI, NA 0.8). An analyzer with polarization direction along the vertical axis of the sample plane and a rotatable polarizer were used to characterize orientation-dependent plasmonic light scattering.

Confocal fluorescence imaging of QR arrays was conducted on a home-built microscopy setup using a Zeiss Eclipse TI microscope body with a piezo controlled 3D movable sample stage and a 100× air objective (Nikon MUE42900, NA 0.9). Arrays were excited using a 488 nm laser as the sample was moved in a raster scanning pattern using a piezoelectric stage. Circularly polarized excitation light was achieved using a wire grid linear polarizer (ThorLabs WP25M-VIS) and quarter waveplate (ThorLabs AQWP05M-600). Emission light was filtered using a 506 nm single-edge dichroic (Semrock FF506-Di03) and a 500 nm long pass emission filter (ThorLabs FELH0500) followed by a wire grid linear polarizer (ThorLabs WP25M-VIS) on a rotatable mount, rotated in 20-degree increments between scans. The filtered emission was directed through a telescopic 1:1 pinhole system (20 cm lenses, 50 µm pinhole). The final signal was collected on a silicon avalanche photodiode and read out by a time-correlated single photon counting system (Picoquant Hydraharp) communicating with software (Picoquant Symphotime 64) which rendered the confocal images. Widefield PL imaging was conducted on a previously reported home-built microscope setup[111] at room temperature. A lens focused on the back focal plane of the sample was used to convert a 532 nm laser into widefield illumination. Images were collected by an electron-multiplying charge-coupled device (EMCCD) camera (Andor).

Data processing

Detailed image processing methods to acquire sizes, yields and distributions are described in **Supplementary Note 7**. Image files and raw AFM, SEM and PL files are available in corresponding supplementary files and on the open-source data repository *Dryad*.

Data availability

The data that support the findings of this study and the simulation code are openly available in the Supplementary Information files and on the open-source data repository *Dryad*.

Acknowledgements

M.B., X.L. and C.C. are grateful for funding from the Office of Naval Research (N00014-21-1-4013) and the National Science Foundation (CCF 1956054); R.J.M and X.L. thank the Air Force Office of Scientific Research's Natural Materials and Systems Program (FA9550-23-1-0210) for funding. T.S. thanks the Natural Sciences and Engineering Research Council of Canada (NSERC)

for a Postgraduate Scholarship (doctoral program). J.H. and L.R. thank the National Science Foundation ITE Convergence Accelerator Track I (ITE-2236093) for funding. J.Y.L. was supported by the National Research Foundation of Korea (NRF-2021R1C1C2003554) for this work. This work was performed in part through the use of the facilities of MIT.nano and the Harvard University Center for Nanoscale Systems (CNS).

Author contributions

M.B., R.J.M. and X.L. conceived the research and drafted the manuscript. X.L. developed the methods of CSMOP and the integration of NPs and QRs on patterned silicon chips. X.L. performed and optimized DNA origami design and assembly, materials synthesis, resist cavity fabrication, nanomaterials placement, dark-field microscopy, and AFM characterization. L.R. and J.H. designed and fabricated chips with silicon nitride photonic structures. T.S., A.J. and M.G.B. designed and conducted fluorescence and emission polarization experiments. J.Y.L. developed the computational code and performed kinetic simulations. N.S. conducted SEM characterization. C.C. optimized QR-DNA synthesis. All authors contributed to manuscript writing and revision.

Competing interests

The authors declare no competing interests.

References

1. Elshaari, A.W., Pernice, W., Srinivasan, K., Benson, O. & Zwiller, V. Hybrid integrated quantum photonic circuits. *Nat. Photonics* **14**, 285–298 (2020).
2. Shekhar, S. et al. Roadmapping the next generation of silicon photonics. *Nat. Commun.* **15**, 751 (2024).
3. Pelucchi, E. et al. The potential and global outlook of integrated photonics for quantum technologies. *Nat. Rev. Phys.* **4**, 194-208 (2022).
4. Redjem, W. et al. All-silicon quantum light source by embedding an atomic emissive center in a nanophotonic cavity. *Nat. Commun.* **14**, 3321 (2023).
5. Hollenbach, M. et al. Wafer-scale nanofabrication of telecom single-photon emitters in silicon. *Nat. Commun.* **13**, 7683 (2022).
6. Somaschi, N. et al. Near-optimal single-photon sources in the solid state. *Nat. Photonics* **10**, 340-345 (2016).
7. Uppu, R. et al. Scalable integrated single-photon source. *Sci. Adv.* **6**, eabc8268 (2020).
8. Aharonovich, I. & Prawer, S. Fabrication strategies for diamond based ultra bright single photon sources. *Diamond Relat. Mater.* **19**, 729-733 (2010).
9. Agarwal, K., Rai, H. & Mondal, S. Quantum dots: an overview of synthesis, properties, and applications. *Mater. Res. Express* **10**, 062001 (2023).
10. Gaita-Ariño, A., Luis, F., Hill, S. & Coronado, E. Molecular spins for quantum computation. *Nat. Chem.* **11**, 301-309 (2019).
11. Wasielewski, M.R. et al. Exploiting chemistry and molecular systems for quantum information science. *Nat. Rev. Chem.* **4**, 490-504 (2020).

12. Murray, C.B., Norris, D.J. & Bawendi, M.G. Synthesis and characterization of nearly monodisperse CdE (E = sulfur, selenium, tellurium) semiconductor nanocrystallites. *J. Am. Chem. Soc.* **115**, 8706-8715 (1993).
13. Zhu, H. et al. Synthesis of Zwitterionic CsPbBr3 Nanocrystals with Controlled Anisotropy using Surface-Selective Ligand Pairs. *Adv. Mater.* **35**, 2304069 (2023).
14. Zhao, S. et al. Single photon emission from graphene quantum dots at room temperature. *Nat. Commun.* **9**, 3470 (2018).
15. Almutlaq, J. et al. Engineering colloidal semiconductor nanocrystals for quantum information processing. *Nat. Nanotechnol.* **19**, 1091–1100 (2024).
16. Kloeffel, C. & Loss, D. Prospects for spin-based quantum computing in quantum dots. *Annu. Rev. Condens. Matter Phys.* **4**, 51-81 (2013).
17. Ye, Y., Lin, X. & Fang, W. Room-Temperature Single-Photon Sources Based on Colloidal Quantum Dots: A Review. *Materials* **16**, 7684 (2023).
18. Elsinger, L. et al. Integration of Colloidal PbS/CdS Quantum Dots with Plasmonic Antennas and Superconducting Detectors on a Silicon Nitride Photonic Platform. *Nano Lett.* **19**, 5452-5458 (2019).
19. Wang, X.-D. et al. Waveguide-coupled deterministic quantum light sources and post-growth engineering methods for integrated quantum photonics. *Chip* **1**, 100018 (2022).
20. Dhawan, A.R., Nasilowski, M., Wang, Z., Dubertret, B. & Maitre, A. Fabrication of Efficient Single-Emitter Plasmonic Patch Antennas by Deterministic In Situ Optical Lithography using Spatially Modulated Light. *Adv. Mater.* **34**, e2108120 (2022).
21. Sapienza, L., Davanco, M., Badolato, A. & Srinivasan, K. Nanoscale optical positioning of single quantum dots for bright and pure single-photon emission. *Nat. Commun.* **6**, 7833 (2015).
22. Liu, X. et al. On-chip generation of single-photon circularly polarized single-mode vortex beams. *Sci. Adv.* **9**, eadh0725 (2023).
23. Weng, H.C. et al. Heterogeneous Integration of Solid-State Quantum Systems with a Foundry Photonics Platform. *ACS Photonics* **10**, 3302-3309 (2023).
24. Eich, A. et al. Single-Photon Emission from Individual Nanophotonic-Integrated Colloidal Quantum Dots. *ACS Photonics* **9**, 551-558 (2022).
25. Xing, X. et al. High-resolution combinatorial patterning of functional nanoparticles. *Nat. Commun.* **11**, 6002 (2020).
26. Jiang, M., Kurvits, J.A., Lu, Y., Nurmikko, A.V. & Zia, R. Reusable Inorganic Templates for Electrostatic Self-Assembly of Individual Quantum Dots, Nanodiamonds, and Lanthanide-Doped Nanoparticles. *Nano Lett.* **15**, 5010-5016 (2015).
27. Xie, W. et al. Nanoscale and Single-Dot Patterning of Colloidal Quantum Dots. *Nano Lett.* **15**, 7481-7487 (2015).
28. Zhang, Q. et al. Large ordered arrays of single photon sources based on II–VI semiconductor colloidal quantum dot. *Opt. Express* **16**, 19592-19599 (2008).
29. Barelli, M. et al. Single-Photon Emitting Arrays by Capillary Assembly of Colloidal Semiconductor CdSe/CdS/SiO(2) Nanocrystals. *ACS Photonics* **10**, 1662-1670 (2023).
30. Nguyen, H.A. et al. Deterministic Quantum Light Arrays from Giant Silica-Shelled Quantum Dots. *ACS Appl. Mater. Interfaces* **15**, 4294-4302 (2023).
31. Cheng, G. et al. Single CdSe Quantum Dots Positioned in Nanostructured Heterogeneous Templates: Implications for High-Precision Nanoassembly. *ACS Appl. Nano Mater.* **5**, 5756-5763 (2022).

32. Meng, Y. et al. Deterministic Assembly of Single Sub-20 nm Functional Nanoparticles Using a Thermally Modified Template with a Scanning Nanoprobe. *Adv. Mater.* **32**, 2005979 (2020).
33. Ni, S., Leemann, J., Buttinoni, I., Isa, L. & Wolf, H. Programmable colloidal molecules from sequential capillarity-assisted particle assembly. *Sci. Adv.* **2**, e1501779 (2016).
34. Flauraud, V. et al. Nanoscale topographical control of capillary assembly of nanoparticles. *Nat. Nanotechnol.* **12**, 73-80 (2017).
35. Funke, J.J. & Dietz, H. Placing molecules with Bohr radius resolution using DNA origami. *Nat. Nanotechnol.* **11**, 47-52 (2016).
36. Adamczyk, A.K. et al. DNA Self-Assembly of Single Molecules with Deterministic Position and Orientation. *ACS Nano* **16**, 16924-16931 (2022).
37. Gorman, J. et al. Sculpting photoproducts with DNA origami. *Chem* (2024).
38. Liu, N. & Liedl, T. DNA-assembled advanced plasmonic architectures. *Chem. Rev.* **118**, 3032-3053 (2018).
39. Hartl, C. et al. Position Accuracy of Gold Nanoparticles on DNA Origami Structures Studied with Small-Angle X-ray Scattering. *Nano Lett.* **18**, 2609-2615 (2018).
40. Glembockyte, V., Grabenhorst, L., Trofymchuk, K. & Tinnefeld, P. DNA Origami Nanoantennas for Fluorescence Enhancement. *Acc. Chem. Res.* **54**, 3338-3348 (2021).
41. Ge, H. et al. Sequence-Dependent DNA Functionalization of Upconversion Nanoparticles and Their Programmable Assemblies. *Angew. Chem. Int. Ed.* **59**, 8133-8137 (2020).
42. Chen, C. et al. Nanoscale 3D spatial addressing and valence control of quantum dots using wireframe DNA origami. *Nat. Commun.* **13**, 4935 (2022).
43. Chen, C. et al. Ultrafast dense DNA functionalization of quantum dots and rods for scalable 2D array fabrication with nanoscale precision. *Sci. Adv.* **9**, eadh8508 (2023).
44. Huang, D., Haddad, L., Rahman, F., Palma, M. & Sapelkin, A. Engineering a DNA origami mediated multicolour quantum dot platform for sub-diffraction spectral separation imaging. *RSC Advances* **12**, 23778-23785 (2022).
45. Ko, S.H., Du, K. & Liddle, J.A. Quantum-dot fluorescence lifetime engineering with DNA origami constructs. *Angew. Chem. Int. Ed. Engl.* **52**, 1193-1197 (2013).
46. Bui, H. et al. Programmable periodicity of quantum dot arrays with DNA origami nanotubes. *Nano Lett.* **10**, 3367-3372 (2010).
47. Gür, F.N. et al. DNA-Assembled Plasmonic Waveguides for Nanoscale Light Propagation to a Fluorescent Nanodiamond. *Nano Lett.* **18**, 7323-7329 (2018).
48. Zhang, T. et al. DNA-Based Self-Assembly of Fluorescent Nanodiamonds. *J. Am. Chem. Soc.* **137**, 9776-9779 (2015).
49. Kershner, R.J. et al. Placement and orientation of individual DNA shapes on lithographically patterned surfaces. *Nat. Nanotechnol.* **4**, 557-561 (2009).
50. Gopinath, A. & Rothemund, P.W.K. Optimized Assembly and Covalent Coupling of Single-Molecule DNA Origami Nanoarrays. *ACS Nano* **8**, 12030-12040 (2014).
51. Gopinath, A., Miyazono, E., Faraon, A. & Rothemund, P.W.K. Engineering and mapping nanocavity emission via precision placement of DNA origami. *Nature* **535**, 401-405 (2016).
52. Gopinath, A. et al. Absolute and arbitrary orientation of single-molecule shapes. *Science* **371**, eabd6179 (2021).
53. Martynenko, I.V. et al. Site-directed placement of three-dimensional DNA origami. *Nat. Nanotechnol.* **18**, 1456-1462 (2023).

54. Sikeler, C., Haslinger, F., Martynenko, I.V. & Liedl, T. DNA Origami-Directed Self-Assembly of Gold Nanospheres for Plasmonic Metasurfaces. *Adv. Funct. Mater.* **34**, 2404766 (2024).
55. Huang, D., Freeley, M. & Palma, M. DNA-Mediated Patterning of Single Quantum Dot Nanoarrays: A Reusable Platform for Single-Molecule Control. *Sci. Rep.* **7**, 45591 (2017).
56. Scheible, M.B., Pardatscher, G., Kuzyk, A. & Simmel, F.C. Single Molecule Characterization of DNA Binding and Strand Displacement Reactions on Lithographic DNA Origami Microarrays. *Nano Lett.* **14**, 1627-1633 (2014).
57. Gerdon, A.E. et al. Controlled Delivery of DNA Origami on Patterned Surfaces. *Small* **5**, 1942-1946 (2009).
58. Penzo, E., Wang, R., Palma, M. & Wind, S.J. Selective placement of DNA origami on substrates patterned by nanoimprint lithography. *J. Vac. Sci. Technol. B* **29**, 06F205 (2011).
59. Brassat, K. et al. On the Adsorption of DNA Origami Nanostructures in Nanohole Arrays. *Langmuir* **34**, 14757-14765 (2018).
60. Shetty, R.M., Brady, S.R., Rothemund, P.W.K., Hariadi, R.F. & Gopinath, A. Bench-Top Fabrication of Single-Molecule Nanoarrays by DNA Origami Placement. *ACS Nano* **15**, 11441-11450 (2021).
61. Pirandola, S., Bardhan, B.R., Gehring, T., Weedbrook, C. & Lloyd, S. Advances in photonic quantum sensing. *Nat. Photonics* **12**, 724-733 (2018).
62. Zhong, H.-S. et al. Quantum computational advantage using photons. *Science* **370**, 1460-1463 (2020).
63. Luo, W. et al. Recent progress in quantum photonic chips for quantum communication and internet. *Light Sci. Appl.* **12**, 175 (2023).
64. Zhou, Y. et al. Shape-Selective Deposition and Assembly of Anisotropic Nanoparticles. *Nano Lett.* **14**, 2157-2161 (2014).
65. Zhou, W. et al. Device-quality, reconfigurable metamaterials from shape-directed nanocrystal assembly. *Proc. Natl. Acad. Sci. U.S.A.* **117**, 21052-21057 (2020).
66. Jun, H., Wang, X., Bricker, W.P. & Bathe, M. Automated sequence design of 2D wireframe DNA origami with honeycomb edges. *Nat. Commun.* **10**, 5419 (2019).
67. Wang, X. et al. Planar 2D wireframe DNA origami. *Sci. Adv.* **8**, eabn0039 (2022).
68. Wagenbauer, K.F. et al. How We Make DNA Origami. *ChemBioChem* **18**, 1873-1885 (2017).
69. Shaw, A., Benson, E. & Högberg, B. Purification of Functionalized DNA Origami Nanostructures. *ACS Nano* **9**, 4968-4975 (2015).
70. Tapio, K. et al. Large-Scale Formation of DNA Origami Lattices on Silicon. *Chem. Mater.* **35**, 1961-1971 (2023).
71. Woo, S. & Rothemund, P.W.K. Self-assembly of two-dimensional DNA origami lattices using cation-controlled surface diffusion. *Nat. Commun.* **5**, 4889 (2014).
72. Xin, Y., Martinez Rivadeneira, S., Grundmeier, G., Castro, M. & Keller, A. Self-assembly of highly ordered DNA origami lattices at solid-liquid interfaces by controlling cation binding and exchange. *Nano Res.* **13**, 3142-3150 (2020).
73. Lin, Q.-Y. et al. Building superlattices from individual nanoparticles via template-confined DNA-mediated assembly. *Science* **359**, 669-672 (2018).
74. Zheng, J. et al. Gold Nanorods: The Most Versatile Plasmonic Nanoparticles. *Chem. Rev.* **121**, 13342-13453 (2021).

75. Kuemin, C., Nowack, L., Bozano, L., Spencer, N.D. & Wolf, H. Oriented Assembly of Gold Nanorods on the Single-Particle Level. *Adv. Funct. Mater.* **22**, 702-708 (2011).
76. Huang, Y. & Kim, D.H. Dark-field microscopy studies of polarization-dependent plasmonic resonance of single gold nanorods: rainbow nanoparticles. *Nanoscale* **3**, 3228-3232 (2011).
77. Zhang, H. et al. Direct Assembly of Large Area Nanoparticle Arrays. *ACS Nano* **12**, 7529-7537 (2018).
78. Li, Z., Liu, W., Cheng, H., Chen, S. & Tian, J. Manipulation of the Photonic Spin Hall Effect with High Efficiency in Gold-Nanorod-Based Metasurfaces. *Adv. Opt. Mater.* **5**, 1700413 (2017).
79. Cai, J., Zhang, C. & Li, W.-D. Dual-Color Flexible Metasurfaces with Polarization-Tunable Plasmons in Gold Nanorod Arrays. *Adv. Opt. Mater.* **9**, 2001401 (2021).
80. Zijlstra, P., Chon, J.W.M. & Gu, M. Five-dimensional optical recording mediated by surface plasmons in gold nanorods. *Nature* **459**, 410-413 (2009).
81. Taylor, A.B., Michaux, P., Mohsin, A.S.M. & Chon, J.W.M. Electron-beam lithography of plasmonic nanorod arrays for multilayered optical storage. *Opt. Express* **22**, 13234-13243 (2014).
82. Liu, M. et al. Colloidal quantum dot electronics. *Nat. Electron.* **4**, 548-558 (2021).
83. Shirasaki, Y., Supran, G.J., Bawendi, M.G. & Bulović, V. Emergence of colloidal quantum-dot light-emitting technologies. *Nat. Photonics* **7**, 13-23 (2012).
84. Kagan, C.R., Bassett, L.C., Murray, C.B. & Thompson, S.M. Colloidal Quantum Dots as Platforms for Quantum Information Science. *Chem. Rev.* **121**, 3186-3233 (2021).
85. Li, L.-s., Hu, J., Yang, W. & Alivisatos, A.P. Band Gap Variation of Size- and Shape-Controlled Colloidal CdSe Quantum Rods. *Nano Lett.* **1**, 349-351 (2001).
86. Srivastava, A.K., Zhang, W., Schneider, J., Halpert, J.E. & Rogach, A.L. Luminescent Down-Conversion Semiconductor Quantum Dots and Aligned Quantum Rods for Liquid Crystal Displays. *Adv. Sci.* **6**, 1901345 (2019).
87. Zhang, Q. et al. Perovskite Light-Emitting Diodes with Quantum Wires and Nanorods. *Adv. Mater.*, 2405418 (2024).
88. Pisanello, F. et al. Dots in rods as polarized single photon sources. *Superlattices Microstruct.* **47**, 165-169 (2010).
89. Jing, X. et al. Solidifying framework nucleic acids with silica. *Nat. Protoc.* **14**, 2416-2436 (2019).
90. Liu, X. et al. Complex silica composite nanomaterials templated with DNA origami. *Nature* **559**, 593-598 (2018).
91. Wassermann, L.M., Scheckenbach, M., Baptist, A.V., Glembockyte, V. & Heuer-Jungemann, A. Full Site-Specific Addressability in DNA Origami-Templated Silica Nanostructures. *Adv. Mater.* **35**, 2212024 (2023).
92. Yuan, G., Gomez, D.E., Kirkwood, N., Boldt, K. & Mulvaney, P. Two Mechanisms Determine Quantum Dot Blinking. *ACS Nano* **12**, 3397-3405 (2018).
93. Galland, C. et al. Two types of luminescence blinking revealed by spectroelectrochemistry of single quantum dots. *Nature* **479**, 203-207 (2011).
94. Mahler, B. et al. Towards non-blinking colloidal quantum dots. *Nat. Mater.* **7**, 659-664 (2008).
95. Chen, O. et al. Compact high-quality CdSe-CdS core-shell nanocrystals with narrow emission linewidths and suppressed blinking. *Nat. Mater.* **12**, 445-451 (2013).

96. Shi, J. et al. All-optical fluorescence blinking control in quantum dots with ultrafast mid-infrared pulses. *Nat. Nanotechnol.* **16**, 1355-1361 (2021).
97. le Feber, B., Prins, F., De Leo, E., Rabouw, F.T. & Norris, D.J. Colloidal-Quantum-Dot Ring Lasers with Active Color Control. *Nano Lett.* **18**, 1028-1034 (2018).
98. Weeber, J.-C. et al. Colloidal quantum dots decorated micro-ring resonators for efficient integrated waveguides excitation. *Nanophotonics* **9**, 1411-1423 (2020).
99. Ma, J. et al. Engineering Quantum Light Sources with Flat Optics. *Adv. Mater.* **36**, 2313589 (2024).
100. Peniakov, G. et al. Polarized and Unpolarized Emission from a Single Emitter in a Bullseye Resonator. *Laser Photonics Rev.* **18**, 2300835 (2024).
101. Zhang, X. et al. Adsorption of DNA Oligonucleotides by Titanium Dioxide Nanoparticles. *Langmuir* **30**, 839-845 (2014).
102. Kaminska, I. et al. Distance Dependence of Single-Molecule Energy Transfer to Graphene Measured with DNA Origami Nanopositioners. *Nano Lett.* **19**, 4257-4262 (2019).
103. Jin, Z. et al. Metallized DNA nanolithography for encoding and transferring spatial information for graphene patterning. *Nat. Commun.* **4**, 1663 (2013).
104. Park, H.-Y. et al. n- and p-Type Doping Phenomenon by Artificial DNA and M-DNA on Two-Dimensional Transition Metal Dichalcogenides. *ACS Nano* **8**, 11603-11613 (2014).
105. Wang, J., Sciarrino, F., Laing, A. & Thompson, M.G. Integrated photonic quantum technologies. *Nat. Photonics* **14**, 273-284 (2020).
106. Jun, H. et al. Rapid prototyping of arbitrary 2D and 3D wireframe DNA origami. *Nucleic Acids Res.* **49**, 10265-10274 (2021).
107. Wang, X., Jun, H. & Bathe, M. Programming 2D Supramolecular Assemblies with Wireframe DNA Origami. *J. Am. Chem. Soc.* **144**, 4403–4409 (2022).
108. Liu, B. & Liu, J. Freezing Directed Construction of Bio/Nano Interfaces: Reagentless Conjugation, Denser Spherical Nucleic Acids, and Better Nanoflares. *J. Am. Chem. Soc.* **139**, 9471-9474 (2017).
109. Bastús, N.G., Comenge, J. & Puntes, V. Kinetically Controlled Seeded Growth Synthesis of Citrate-Stabilized Gold Nanoparticles of up to 200 nm: Size Focusing versus Ostwald Ripening. *Langmuir* **27**, 11098-11105 (2011).
110. Hao, Y., Li, Y., Song, L. & Deng, Z. Flash Synthesis of Spherical Nucleic Acids with Record DNA Density. *J. Am. Chem. Soc.* **143**, 3065-3069 (2021).
111. Harris, I.B.W. et al. Hyperfine Spectroscopy of Isotopically Engineered Group-IV Color Centers in Diamond. *PRX Quantum* **4**, 040301 (2023).